

Analysis of Test Case Computations and Experiments for the First Aeroelastic Prediction Workshop

David M. Schuster¹

NASA Engineering and Safety Center, Hampton, VA, 23681

Pawel Chwalowski², Jennifer Heeg³, and Carol Wieseman⁴

NASA Langley Research Center, Hampton, VA 23681

This paper compares computational and experimental data from the first Aeroelastic Prediction Workshop (AePW) held in April, 2012. The workshop has been designed as a series of technical interchange meetings to assess the state of the art of computational methods for predicting unsteady flowfields and static and dynamic aeroelastic response. The goals are to provide an impartial forum to evaluate the effectiveness of existing computer codes and modeling techniques to simulate aeroelastic problems, and to identify computational and experimental areas needing additional research and development. For this initial workshop, three subject configurations were chosen from existing wind tunnel data sets where there is pertinent experimental data available for comparison. Participant researchers analyzed one or more of the subject configurations and results from all of these computations were compared at the workshop.

Nomenclature

C_p	=	Pressure coefficient
$\text{Re}()$	=	Real component of the unsteady quantity, the component of the unsteady quantity that is in-phase with the wing motion.
$\text{Im}()$	=	Imaginary component of the unsteady quantity, the component of the unsteady quantity that is 90° out-of-phase with the wing motion.
α	=	Angle-of-attack (°)
θ	=	Amplitude of pitch oscillation (°)
Δz	=	Amplitude of HIRENASD wing tip displacement (mm)

I. Introduction

The Aeroelastic Prediction Workshop (AePW)¹ has been patterned after two very successful workshops conducted over the past decade: the Drag Prediction Workshop² and the High Lift Prediction Workshop³. The AePW assembles an international slate of participants to analyze a carefully selected set of unsteady aerodynamics and aeroelastic problems for which experimental validation data is available. The intent of the workshop is to investigate the ability of present computational tools to predict nonlinear aeroelastic phenomena, particularly those arising from the formation of shock waves, vortices, and separated flow. A thorough description of the workshop formation and execution can be found in Reference 1.

In June, 2011, the AePW was formally initiated at the International Forum on Aeroelasticity and Structural Dynamics held in Paris, France⁴. At this meeting, the objectives of the workshop and pertinent information required to participate in the event were provided to prospective analysts. A website was established (<https://c3.nasa.gov/dashlink/projects/47/>) where analysts and other interested parties could obtain participation information, modeling and analysis guidelines, test case configuration data, experimental comparison data, computational grids, and other reference materials. This public site is still in operation today, and now contains a

¹ NASA Technical Fellow for Aerosciences, MS 431, Associate Fellow, AIAA.

² Insert Job Title, Department Name, Address/Mail Stop, and AIAA Member Grade for third author.

³ Insert Job Title, Department Name, Address/Mail Stop, and AIAA Member Grade for fourth author (etc).

⁴ Insert Job Title, Department Name, Address/Mail Stop, and AIAA Member Grade for fourth author (etc).

record of the analyses completed for the first AePW and future AePW plans. Computational grids for the various configurations were developed by the AePW Organizing Committee (OC) and distributed to the registered workshop participants. Participants analyzed the three workshop configurations for approximately nine months, submitting their results in March, 2012. The AePW itself was held on April 21-22 in Honolulu, Hawaii, just prior to the AIAA 53rd Structures, Structural Dynamics, and Materials Conference. The workshop consisted of 59 registered attendees. A total of 17 analysis teams from 10 nations provided a total of 26 analysis datasets for evaluation and comparison.

The first AePW selected three configurations for analysis by the participants:

1. Rectangular Supercritical Wing (RSW)⁵⁻⁸
2. Benchmark Supercritical Wing (BSCW)⁹⁻¹¹
3. High Reynolds Number Aero-Structural Dynamics Wing (HIRENASD)¹²⁻¹⁸

Each of these configurations will be briefly discussed here, but the reader is again directed to Reference 1 for a more complete description of the configuration selection process and each of the test case geometries and available data.

A. Rectangular Supercritical Wing

The Rectangular Supercritical Wing (RSW) was chosen to be the least complex, both geometrically and aerodynamically, of the three test cases for the AePW. The RSW was tested in the NASA Langley Transonic Dynamics Tunnel (TDT) in 1983 and a photograph from that test is shown in Figure 1. Figure 2 shows the geometric characteristics of the RSW. The wing is a simple rectangular planform with a wing tip of rotation. The wing has a span of 48 inches and a chord of 24 inches with a 12% thick supercritical airfoil section that is constant from wing root to tip. The wing is mounted to a relatively small splitter plate that is offset from the wind tunnel wall by approximately 6 inches. For the forced pitch oscillation cases, the wing was pitched about the 46 percent chord location. The wing was assumed to be rigid for all analyses.

This wing was originally chosen for its geometric simplicity and its transonic, but not overly challenging, aerodynamic characteristics. However, an unforeseen interaction of the wind tunnel wall with the experimental data measured on the wing made this case significantly more difficult than anticipated. A calibration of the TDT **Error! Reference source not found.**, conducted after this test was performed shows the wind tunnel boundary layer for the wall on which the model and splitter plate were mounted to be approximately 12 inches thick at RSW test conditions of interest. This places the RSW splitter plate well within the wind tunnel wall boundary layer. The impact of this situation on the wing pressure distribution near the wing root was not appreciated by the AePW Organizing Committee (OC) prior to the wing's selection as a test case. Preliminary AePW analyses of the RSW showed the inboard pressure distributions to be



Figure 1: Rectangular Supercritical Wing mounted in the NASA Langley Transonic Dynamics Tunnel.

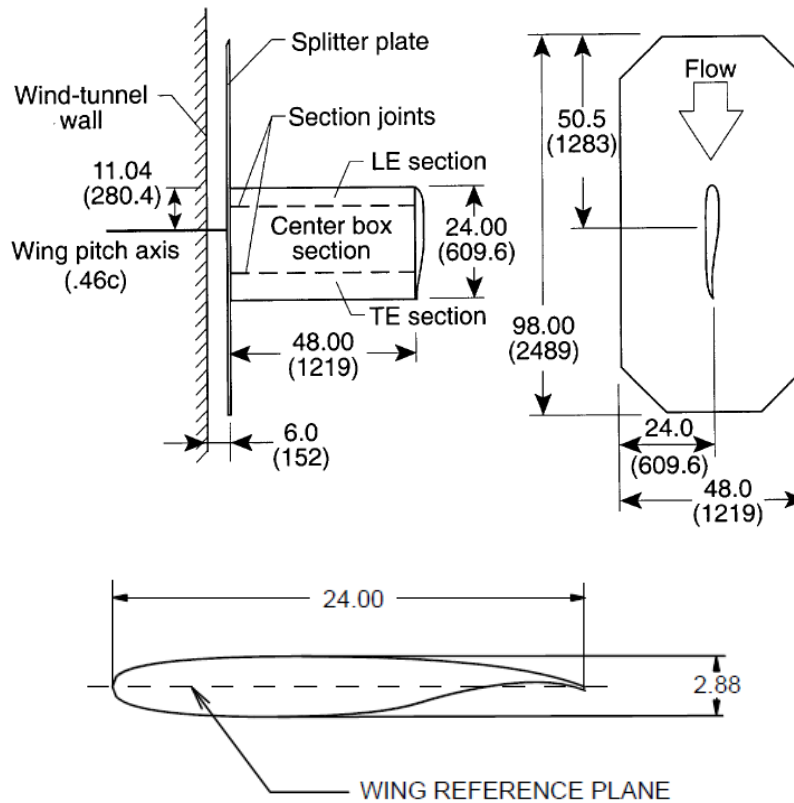


Figure 2: RSW geometric characteristics.

highly affected by the presence of the wind tunnel wall boundary layer. The AePW organizers attempted to account for the wind tunnel wall boundary layer and conducted extensive studies to characterize and correct models for this effect. These efforts are described in detail in Reference 19. Ultimately, the inclusion of the wind tunnel wall boundary layer in the computational analysis made this case much more difficult than anticipated, resulting in significant deviations in comparisons between the CFD methods and the experimental data for the inboard pressure station.

The wing was tested in R-12 heavy gas in the TDT, and all AePW analysts performed their simulations by changing the ratio of specific heats from $\gamma = 1.4$ to $\gamma = 1.132$ to account for the differences in thermodynamic properties between air and R-12. Pressure data were measured at four constant-span stations on the wing, $y/b = 0.308, 0.588, 0.809$, and 0.951 . These pressures include steady pressure coefficients for the static data points and pressure coefficients processed at the frequency of the forced pitch oscillation, in terms of magnitude and phase, for the dynamic data points. Reference 8 further post-processed the original magnitude and phase data into real (in-phase) and imaginary (90 degrees out-of-phase) pressure coefficient components scaled by the wing oscillation amplitude. There were no integrated force or moment measurements conducted in the test.

The AePW OC chose a total of four test cases for analysis by the AePW participants, two steady and two unsteady. Table 1 shows the analysis conditions chosen for the RSW.

Table 1. Rectangular Supercritical Wing analysis conditions.

Mach Number	Mean Angle of Attack (α , deg.)	Pitch Oscillation Frequency (f , Hz)	Pitch Oscillation Amplitude (θ , deg.)	Reduced Frequency $\omega C/(2V_\infty)$	Reynolds Number ($10^6/\text{ft.}$)
0.825	2.0	0	0.0	0.0	2.0
0.825	4.0	0	0.0	0.0	2.0
0.825	2.0	10	1.0	0.152	2.0
0.825	2.0	20	1.0	0.304	2.0

B. Benchmark Supercritical Wing

The Benchmark SuperCritical Wing (BSCW), shown in Figure 3, was chosen as a configuration of similar geometric simplicity to the RSW case, but with flow conditions that would prove more challenging to the AePW analysts. This configuration was chosen because the experiment exhibited highly nonlinear unsteady behavior, specifically shock-separated transient flow. While there are fewer pressure measurements than for the RSW configuration, the time history data records are available for all test conditions. In addition, the BSCW experimental data chosen for this case has not been widely published. It was obtained during check-out testing of the TDT Oscillating Turntable (OTT) hardware and thus was not the focus of a computational research project. While the data is publicly available in graphical form¹¹, it was viewed as obscure enough to serve as the basis for a semi-blind test case. Thus the experimental data was not provided to the AePW participants prior to the actual workshop.

The BSCW has a rectangular planform as shown in Figure 4, with a NASA SC(2)-0414 airfoil. Like the RSW, the BSCW was tested in the TDT. However, the BSCW test was conducted after the TDT's conversion to R-134a as its heavy gas, so the cases for the BSCW were all computed with $\gamma = 1.116$ to account for this new test medium. The model was mounted to a large splitter plate that was offset from the TDT wall so as to place the wing closer to the center of the tunnel test section. This offset was well outside the wind tunnel wall boundary layer, so the BSCW avoided the issues with the wall boundary layer encountered on the RSW. The testing was also conducted with the sidewall slots closed, a technique which has been shown to improve the prediction of force and moment coefficients when semispan models are mounted directly to the TDT wall. The model's instrumentation is limited to one row of 40 in-situ unsteady pressure transducers at the 60% span station.

Dynamic data was obtained for the BSCW by oscillating the model in a pitching motion about the 30% chord. Steady information pertinent to this configuration is calculated as the mean value from the oscillatory time histories. The data processing performed shows small variations in the mean data due to the forcing frequency. These variations were treated as uncertainties in the steady experimental information. The analysis conditions chosen for the BSCW are shown in Table 2.

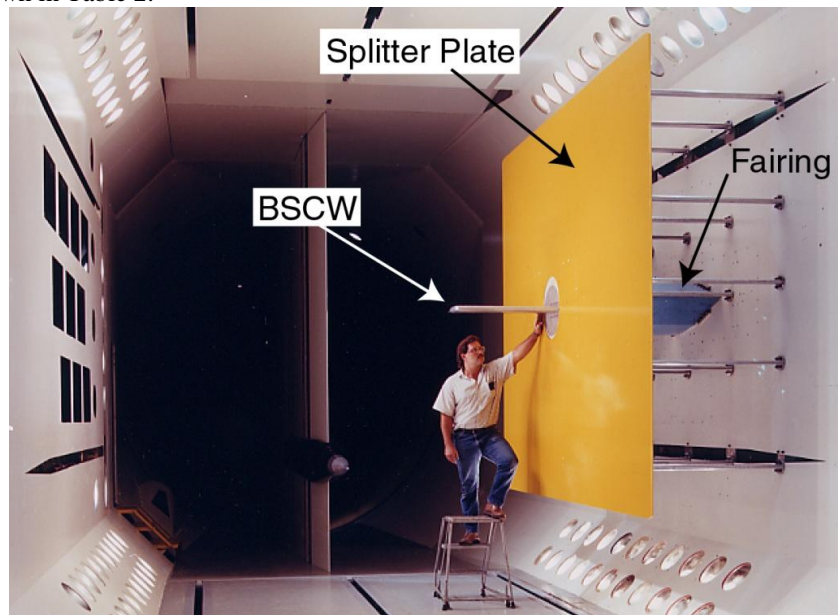


Figure 3: Benchmark Supercritical Wing mounted in the NASA Langley Transonic Dynamics Tunnel.

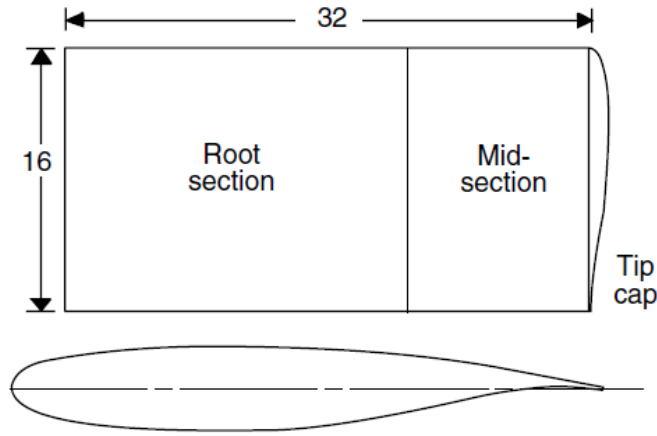


Figure 4: Planform and airfoil section for the Benchmark Supercritical Wing.

Table 2. Benchmark Supercritical Wing analysis conditions.

Mach Number	Mean Angle of Attack (α , deg.)	Pitch Oscillation Frequency (f , Hz)	Pitch Oscillation Amplitude (θ , deg.)	Reduced Frequency $\omega C/(2V_\infty)$	Reynolds Number ($10^6/\text{ft.}$)
0.85	5.0	0	0.0	0.0	3.4
0.85	5.0	1	1.0	0.007	3.4
0.85	5.0	10	1.0	0.067	3.4

C. High Reynolds Number Aero-Structural Dynamics Wing

The High Reynolds Number Aero-Structural Dynamics (HIRENASD) model was the final configuration chosen for analysis in the first AePW. This model was chosen as an initial coupled aeroelastic analysis configuration. The wing has a high degree of structural stiffness and broad spacing of the structural modes, which produces weak aeroelastic coupling and makes it a good entry-level basis of evaluation. The additional benefits of this data set are availability of time histories and expertise from the experimentalists who are part of the AePW OC. Portions of the HIRENASD data set have been previously publicized, distributed, and analyzed¹²⁻¹⁸.

HIRENASD was tested in the European Transonic Wind tunnel (ETW) in 2007. The model, as installed in this facility, is shown in Figure 5, and described by References 12-14. The model has a 34 degree aft-swept, tapered clean wing, with a BAC 3-11 supercritical airfoil profile. The test article is a semi-span model, ceiling-mounted through a non-contacting fuselage fairing to a turntable, balance and excitation system, shown in Figure 6. The model and balance were designed to be very stiff, with well-separated modes. The first two wing bending modes have frequencies of approximately 27 and 79 Hz; the first wing torsion mode has a frequency of approximately 265 Hz. The model's instrumentation includes 259 in-situ unsteady pressure transducers at 7 span stations. In addition to the unsteady pressures, balance measurements and accelerations were obtained. For a small set of data points, wing displacements were also extracted via stereo pattern tracking.



Figure 5: HIRENASD wing mounted in the European Transonic Wind Tunnel.

Two types of testing were conducted: angle-of-attack polars and forced oscillations. The angle-of-attack polar data was obtained by slowly varying the angle of attack at an angular sweep rate of 0.2 degrees/second, holding all other operational parameters constant. These data were utilized primarily to provide static pressure distributions at a given test condition. The forced oscillation data was obtained by differential forcing at a specified modal frequency. All forced oscillation data to be used in the current workshop was excited near the wing's second bending modal frequency. Two Reynolds numbers, 7.0 million and 23.5 million based on reference chord, were analyzed by the AePW participants. Cases were chosen at two Mach numbers, 0.70 and 0.80. The lower Reynolds number case has an angle of attack of 1.5 degrees, while a more challenging angle of attack of -1.34 degrees, corresponding to the zero-lift condition, was selected for analysis at the higher Reynolds number. At Mach 0.7, only the lower Reynolds number data was analyzed and this case was selected as a simpler case with no appreciable aerodynamic nonlinearity. Both the low and high Reynolds numbers were computed at the more challenging 0.80 Mach number. All tests were conducted with nitrogen ($\gamma = 1.4$) as the test medium. Analysis conditions chosen for the HIRENASD wing are shown in Table 3.

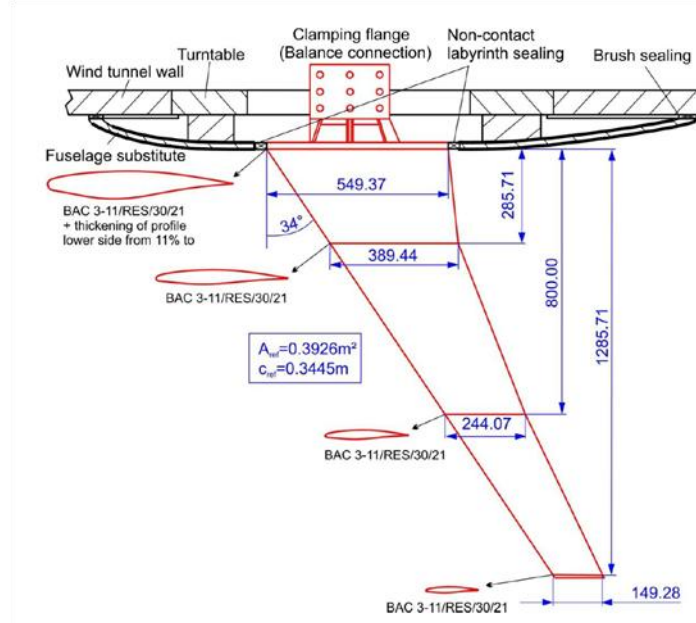


Figure 6: HIRENASD wing planform, dimensions in mm unless otherwise noted.

Table 3. HIRENASD wing analysis conditions.

Mach Number	Mean Angle of Attack (α , deg.)	Forcing Frequency (f , Hz)	2 nd Bending Amplitude (Δz_t , mm)	Chord Reynolds Number ($\times 10^6$)
0.70	1.5	0	0.0	7.0
0.80	1.5	0	0.0	7.0
0.80	-1.34	0	0.0	23.5
0.70	1.5	79.3	2.0	7.0
0.80	1.5	78.9	2.4	7.0
0.80	-1.34	80.4	0.9	23.5

D. Workshop Data

Comparison of steady and unsteady pressure coefficient data for each of the three configurations is the primary focus of this paper. Integrated loads data for each of the configurations was collected from the analysts as well, but only the HIRENASD test measured forces and moments experimentally. For the steady cases, the steady pressure coefficient is compared with experimental data at select span stations on each wing. For the unsteady cases, the frequency response of the fluctuating pressure coefficient time histories are computed at the wing excitation frequency and the real and imaginary components of the response function are compared with corresponding experimental data. The unsteady pressure coefficient is normalized by the wing oscillation amplitude in degrees for the RSW and BSCW pitch oscillation cases, and by the tip deflection, in millimeters, for the HIRENASD cases. In the present nomenclature, the real part of the fluctuating pressure coefficient is that component which is in phase with the wing motion, while the imaginary part is the component that is ninety degrees out of phase with the motion.

Depending on the configuration, between 6 and 14 analysts performed computations on each case. This paper examines all submissions for a particular case as a whole, and does not try to split out variations in computational algorithm, grid refinement, turbulence modeling, or temporal refinement. A sample of available computational data for the RSW wing is shown in

Figure 7. The right side of the figure shows the pressure distributions from all of the analysts who computed the $M = 0.825$, $\alpha = 2.0^\circ$ steady case at the $\eta = 0.309$ span station. In this figure, each analyst's computation is depicted with identical solid lines with no distinction between individual analysts, computational algorithm, grid refinement, turbulence model or other distinguishing feature between the computations. The plot represents the total variation in

the predictions of the case at this station from all of the AePW submissions. To simplify the display of the data and facilitate further analysis, the submitted data was further processed to compute an average pressure distribution from all the analyst submissions, along with an envelope around the average that encompasses all of the predictions, as shown in the right hand figure. In this figure, the solid lines represent the upper surface pressure distribution and the dashed lines depict the lower surface pressures. In each, the dark line is the mean of all the submissions and the lighter lines are the envelope around the mean. This approach provides a less cluttered summary of the CFD performance for this case, distinctly showing where the methods consistently predict similar behavior and where they differ. In some cases, the dark mean line may be biased to one side of the envelope. This indicates that for this situation, the majority of the simulations favored the near side of the envelope, while the far side of the envelope was predicted by a minority of the simulations. Biases of this type will be pointed out in the discussion of the data when they occur. For instance, in the right hand plot of

Figure 7, the mean upper surface pressure distribution near 80% chord strongly favors the more negative side of the envelope, indicating that most of the computations were clustered in this vicinity as opposed to the more positive side of the envelope in this vicinity. This technique will be used throughout the remainder of this paper to discuss and analyze the performance of the CFD methods and how they compare with experimental data.

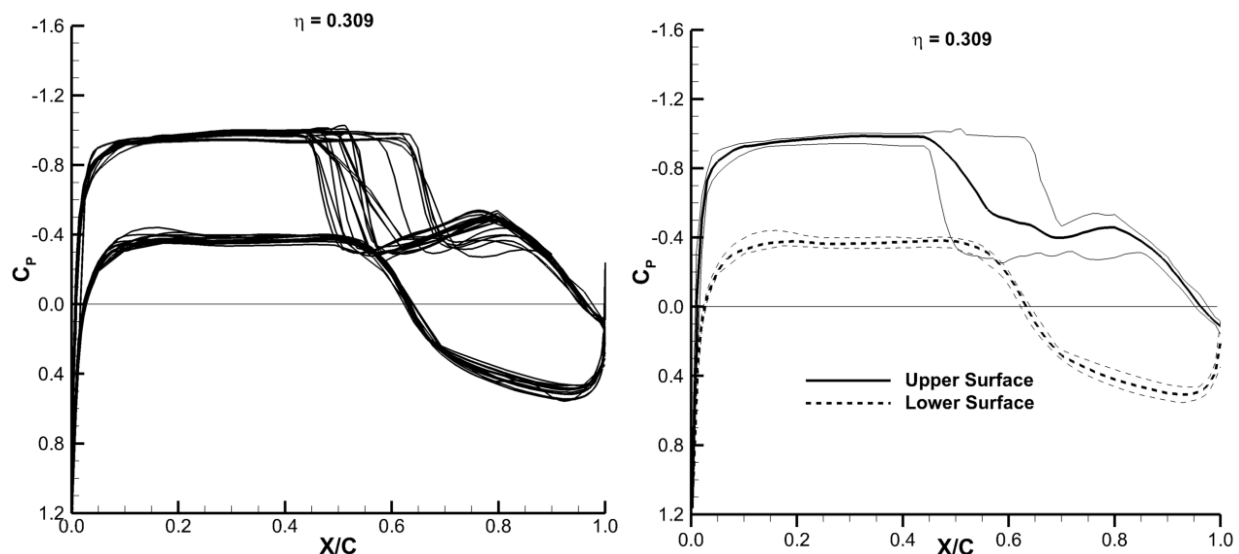


Figure 7. Pressure distribution enveloping technique used in data analysis.

II. AePW Data Analysis

A. Rectangular Supercritical Wing

Six analysts provided results for the RSW using a variety of computational algorithms and grid refinement. For the steady cases, all did a three-level, coarse/medium/fine grid convergence study and most did the same for the unsteady cases. Some of the analysts provided temporal convergence studies for the unsteady cases as well. All computations shown solved the Reynolds Averaged Navier-Stokes (RANS) equations using both structured and unstructured grid formulations. For the RSW, all of the analyses used the Spalart Allmaras turbulence model except for one analyst who used the Menter Shear Stress Turbulence (SST) model.

The steady cases will be discussed first, beginning with the $M = 0.825$, $\alpha = 2.0^\circ$ case. The computed pressure distributions at the $\eta = 0.309$ and 0.809 stations are compared with experimental data in Figure 8. The computations generally predict very consistent results at both wing stations with the exception of the aft upper surface pressure distribution on the inboard wing station. The location of the upper surface shock varies widely at the inboard span station with a total variation in shock location of approximately 20 percent chord. At this station, the results can generally be grouped into two distinct sets, those predicting a forward shock location at approximately 50 percent chord, and those with an aft shock at 65 percent chord. One set of data exhibiting the aft shock location modeled the wing from the splitter plate outboard, with an inviscid wind tunnel wall. This explains the aft shock location predicted for these cases as demonstrated in Reference 19. However, some of the aft shock cases did model the

problem with the viscous wind tunnel wall. An examination of the variation of shock location with grid resolution showed that none of the analysts predicted a shift in the shock location that went from the aft shock set of data to the forward position as a result of improved grid refinement. Most of the computations predict the shock on the outboard station slightly aft of the experimental location, but all of the calculations only vary in location by about 5 percent chord. On the wing lower surface, the computed pressures are very consistent and compare favorably with the experimental data everywhere except aft of about 70 percent chord. This is in the reflexed cove region of the supercritical airfoil section, and it is not clear what may be contributing to these differences, but the pressure magnitude is consistently over-predicted by all of the CFD methods. The outboard wing station is farther away from the area of the wing that was immersed in the wind tunnel wall boundary layer, and the computations and experimental data appear to be less susceptible to this problem at this station.

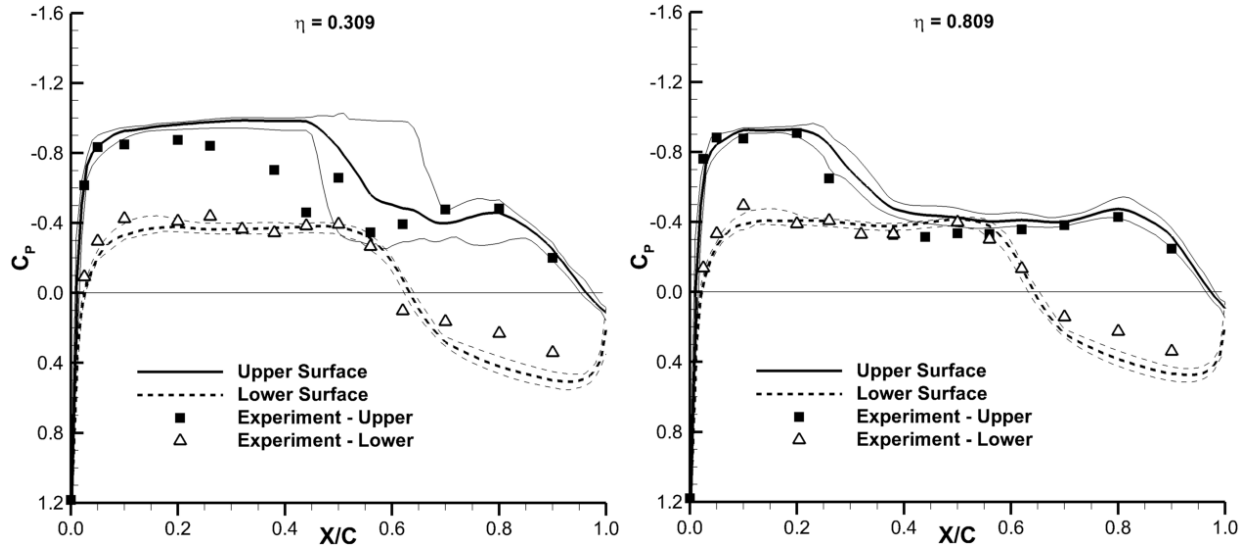


Figure 8. RSW steady pressure comparison $M = 0.825$, $\alpha = 2^\circ$, $\theta = 0.0^\circ$, $f = 0$ Hz.

A similar set of results are presented for the $\alpha = 4^\circ$ case in Figure 9. Again, at the inboard station, the shock location predictions vary widely among the computations with a total spread of approximately 18 percent chord. Forward of the shock on the upper surface, and across the entire lower surface, all of the computations predict very consistent results and compare reasonably well with the experimental data. On the outboard station, most of the computations predict a shock location slightly aft of the experiment with a total variation among the predictions less than five percent chord. The lower surface pressures in the cove region of the wings are again consistently over-predicted by the computations.

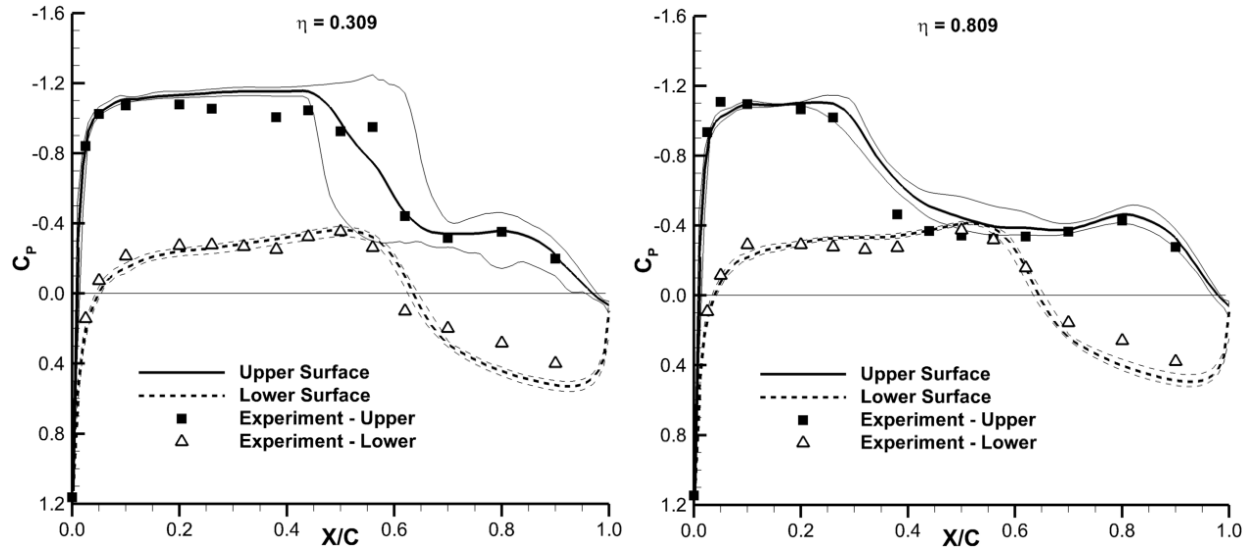


Figure 9. RSW steady pressure comparison $M = 0.825$, $\alpha = 4^\circ$, $\theta = 0.0^\circ$, $f = 0$ Hz.

For the unsteady analyses, the RSW was oscillated in pitch about a steady angle attack of $\alpha = 2^\circ$ with an amplitude of $\theta = 1^\circ$. Two frequencies were investigated, 10 and 20 Hz. Figure 10 compares the computed and experimental unsteady pressure distributions for the $f = 10$ Hz case. The top figures compare results for the $\eta = 0.309$ station, while the bottom plots compare data at the $\eta = 0.809$ station. The real (in-phase) pressure coefficient is shown on the left while the imaginary (out-of-phase) components are shown on the right. At both the inboard and outboard stations, the lower surface fluctuation pressure calculations show good consistency across the various analyses and generally compare favorably with the experimental data. The exception to this is the envelope near the lower surface leading edge on the inboard station. In this area, one of the analyses exhibited some apparent local stability problems that expanded the pressure envelope in this region. The upper surface calculations show good consistency and comparison with the experimental data with envelopes expanding in the vicinity and behind the moving shock wave. The expansion of the envelope is large on the inboard station, due to the influence of the wind tunnel wall boundary layer at this station. The double-lobed distribution in the upper surface envelope is a result of a group of the computations predicting an aft shock location centered just aft of 65% chord, while the larger majority of calculations predicted the shock centered farther forward at about 48% chord. At the inboard station, the envelope of the computations generally contains the experimental data. On the outboard station, away from the influence of the wind tunnel wall boundary layer, the computations show much smaller variation in the vicinity of the upper surface shock centered at approximately 25% chord. However, none of the methods predict the peak real-component amplitude in this region, and only the edge of the computational envelope captures the peak imaginary component amplitude here. Behind the shock on both the inboard and outboard stations, the pressure envelope of the computations spreads as compared to the envelope ahead of the shock. This indicates increased variation in the prediction of the shock/boundary layer interaction and the influence of the prediction of this interaction on the downstream pressure distribution.

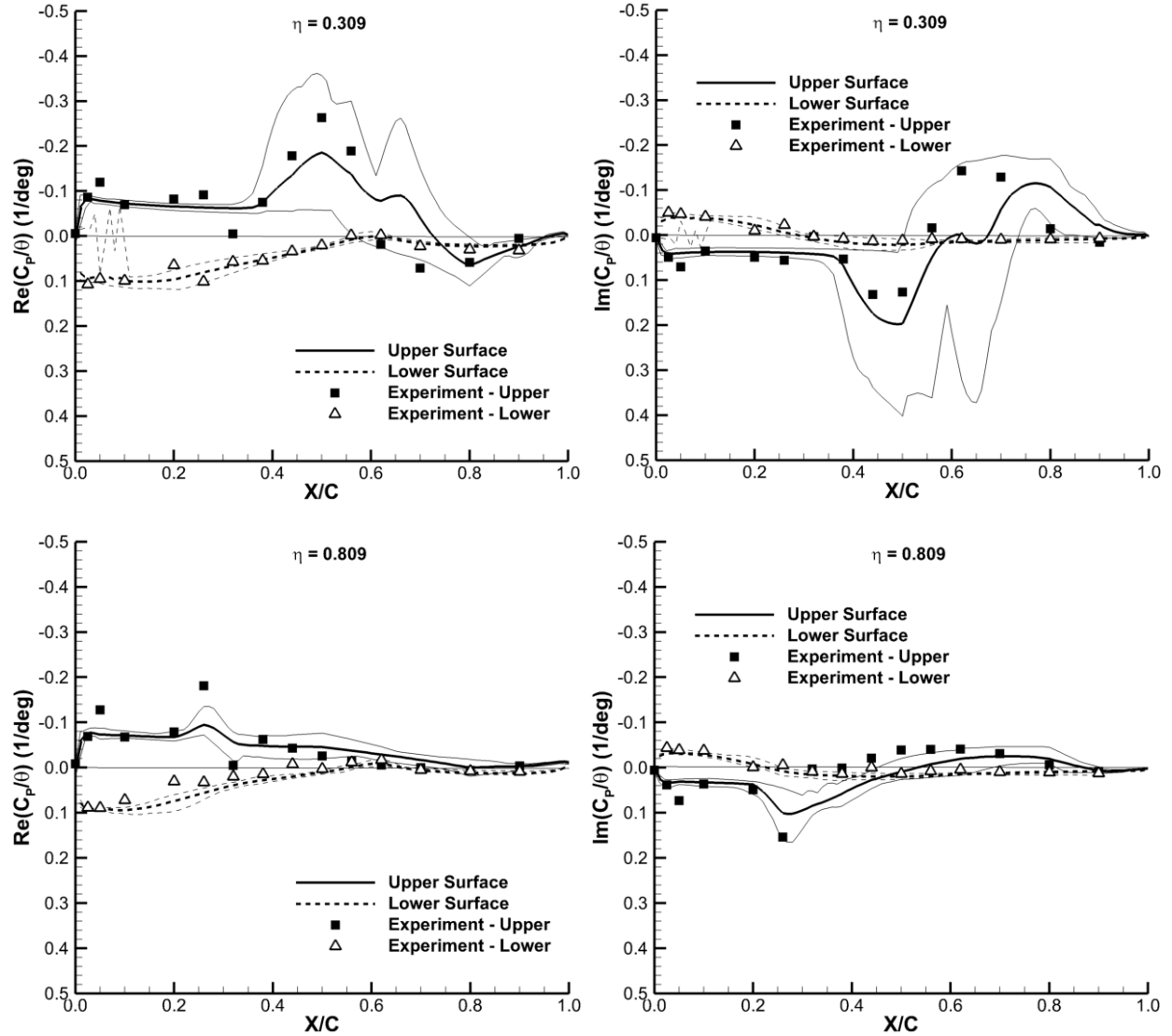


Figure 10. RSW unsteady pressure comparison $M = 0.825$, $\alpha = 2^\circ$, $\theta = 1.0^\circ$, $f = 10$ Hz.

Figure 11 present comparisons for the $f = 20$ Hz. case. In this case, the majority of the upper surface shock motion at the inboard station is out-of-phase with the wing pitch motion as indicated by the increased amplitude of the imaginary component of the pressures at approximately 50% chord. The general character of the computed pressures is similar to that of the $f = 10$ Hz case with the variation across the methods small on the lower surface and ahead of the shock and the variation expanding near and aft of the shock. Comparisons with the experimental data on the outboard wing station and on the inboard station lower surface and ahead of the inboard upper surface shock can be classified as good. Near and aft of the shock on the inboard station upper surface, the experimental pressures are enveloped by the computations, but the variation in the computed data is large due again to the interaction with the wind tunnel wall boundary layer in this region.

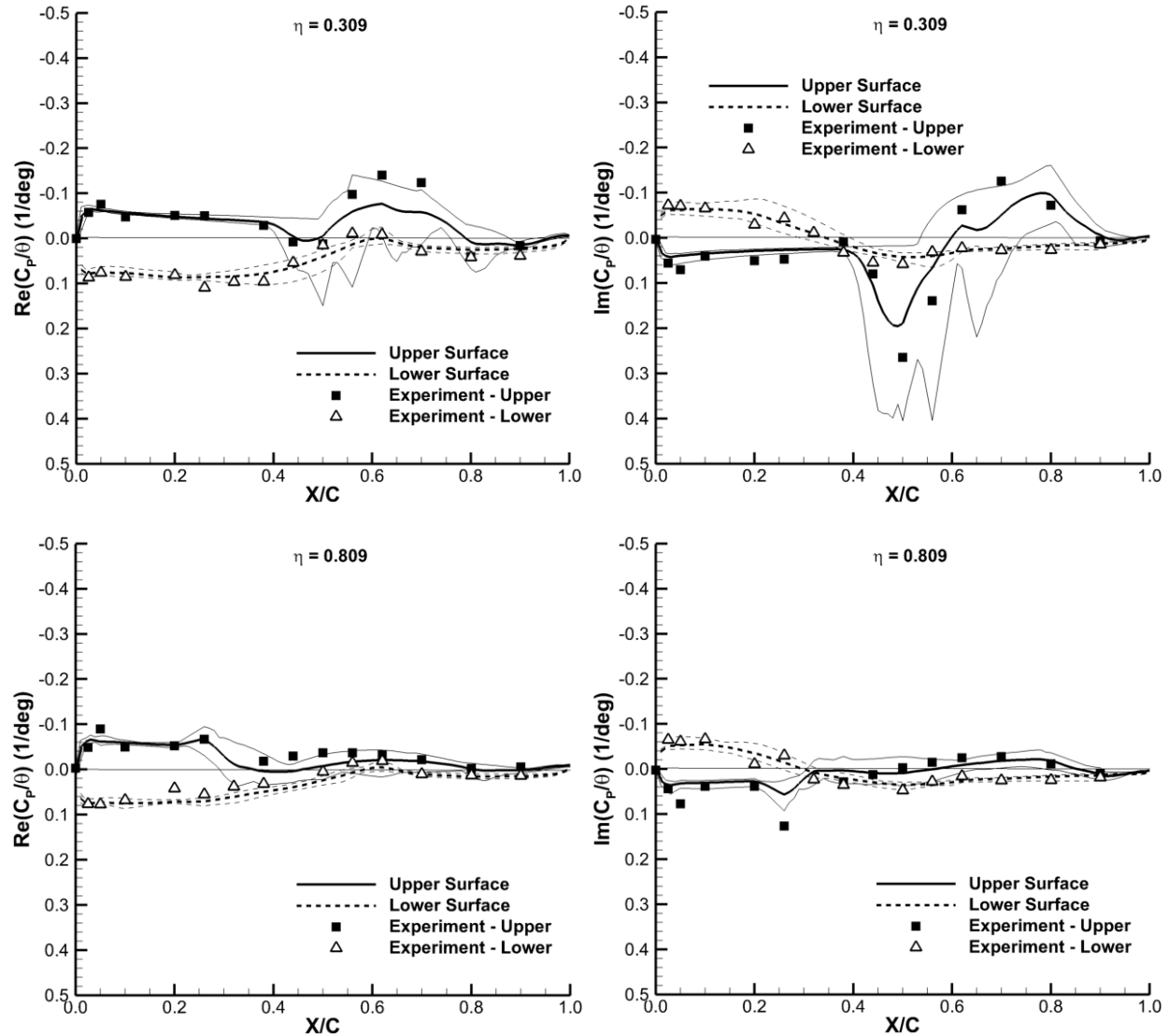


Figure 11. RSW unsteady pressure comparison $M = 0.825$, $\alpha = 2^\circ$, $\theta = 1.0^\circ$, $f = 20$ Hz.

B. Benchmark Supercritical Wing

The Benchmark Supercritical Wing (BSCW) was chosen because it has a simple wing planform, there is recent comprehensive unsteady experimental data available, and these data exhibit some strong nonlinear aerodynamic phenomena. In addition, these recent data have not been widely published making it a nearly blind test case for the AePW participants. The test case was centered on a single Mach number/angle of attack combination with $M = 0.85$, and $\alpha = 5.0^\circ$ as previously shown in Table 2. AePW participants were not supplied with the experimental data prior to performing their computations. Each analyst performed an initial set of computations at a steady angle of attack to provide an initial condition for the unsteady forced pitch oscillation simulation. The results of these steady angle of attack computations at the 60 percent wing span station are shown in Figure 12. As with the RSW case, the BSCW computations show very little variation among the participants across the lower surface of the wing and on the upper surface forward of the predicted shock location. On the upper surface, the computations compare very favorably with the experimental data up to approximately 45 percent chord. Complete time histories are available for this set of experimental data and observed maximum and minimum pressures at each of the transducer locations can be extracted from the pressure time history data. At approximately 45 percent chord, the experimental data indicates a large increase in the difference between the maximum and minimum pressure coefficient, which is indicative of unsteady shock motion. The pressure transducers located at the 40 and 50 percent chord locations

show a much smaller difference between the maximum and minimum pressures, suggesting that the shock oscillation is confined to the region between these two sensors. The large majority of the computations predict a shock location of between 50 and 60 percent chord, somewhat aft of this point. The shock location varies approximately 10% chord across all the participants, with the mean position at about 53% chord. The majority of the methods also predict similar post shock behavior, though at an elevated pressure from the experiment. On the lower surface, the computations produce very consistent results up to the shock and like the RSW case, they tend to over-predict the pressures in the cove region of the supercritical airfoil. The computed differences in the lower surface shock location are not as widespread as on the upper surface.

The AePW analysts indicated that the static angle of attack simulations produced a mixture of steady and unsteady flow. Many of the coarse grid simulations converged to a steady state, while as the grid was refined to the finer grids, the static solutions became unsteady. Upper surface shock-induced boundary layer separation is believed to be the root cause for this unsteadiness in the static data. This forced many of the analysts to employ an unsteady CFD analysis of the static angle of attack case, as opposed to a steady state simulation. The unsteadiness in the static angle of attack data and the varied approaches of the AePW analysts to simulate this problem are what likely lead to the wide variation in prediction of the shock location on the upper surface of the wing.

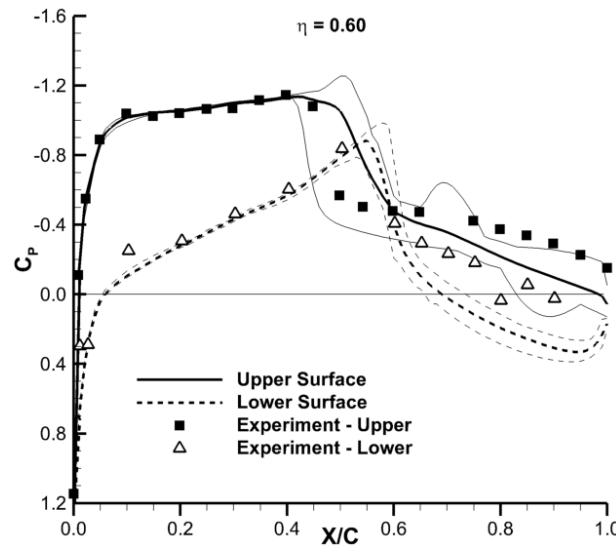


Figure 12. BSCW steady pressure comparison $M = 0.85$, $\alpha = 5^\circ$, $\theta = 0.0^\circ$, $f = 0$ Hz.

Two unsteady forced pitch oscillation cases were investigated, one at a relatively low frequency of 1 Hz and the second at 10 Hz both with an oscillating pitch amplitude of $\theta = 1^\circ$ and a mean angle-of-attack of $\alpha = 5^\circ$. The real and imaginary components of the computed pressure coefficient for the 1 Hz frequency case are compared to the experimental data in Figure 13. The mean real component of the computed data shows an upper surface shock peak at approximately 54% chord, which is well aft of the experimental peak at about 45% chord. The mean of the computed data is also lower in peak amplitude at the upper surface shock location. It is difficult to tell exactly where the experimental peak occurs since it is unlikely that there is a pressure sensor located precisely at the shock location. In this case, it can be inferred from the shape of the pressure distribution that the shock peak occurs somewhere between 45% and 50% chord. Away from the upper surface shock the real component compares very well with the experimental data, including a close prediction of the lower surface shock position and oscillating pressure amplitude. The experimental data shows the unsteady pressure distribution to respond in near perfect phase with the wing motion as evidenced by the very flat, near-zero imaginary component of the pressure coefficient. The mean of the computed data follows this trend closely with only small out-of-phase components predicted near the upper and lower surface shock locations.

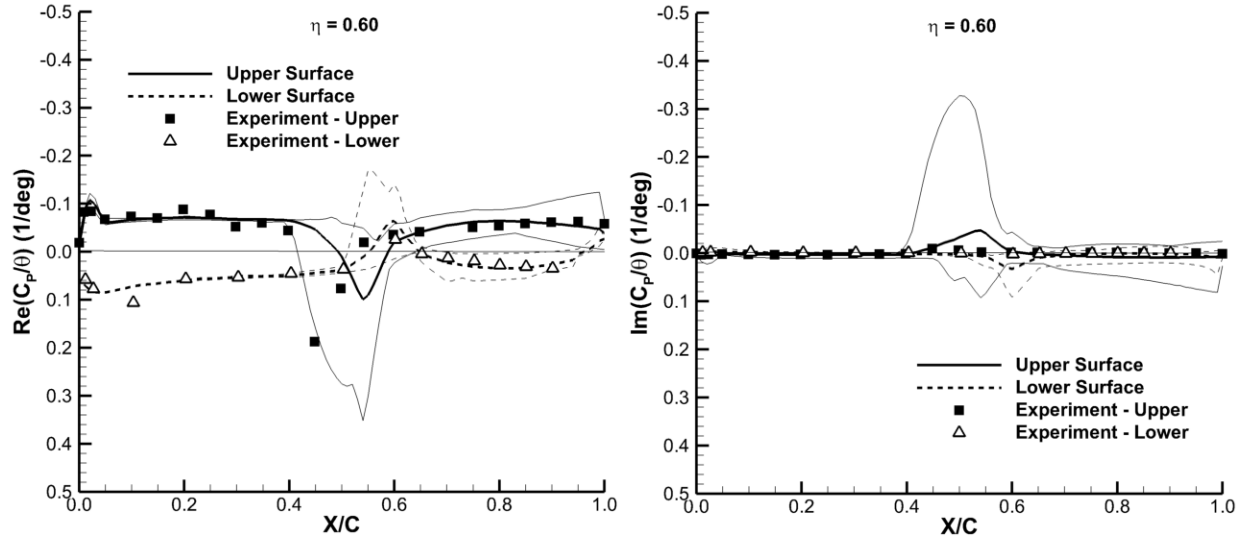


Figure 13. BSCW unsteady pressure comparison $M = 0.85$, $\alpha = 5^\circ$, $\theta = 1.0^\circ$, $f = 1$ Hz.

The results for the 10 Hz Case are shown in Figure 14. Again, it appears that the majority of the AePW analysts are predicting a shock location aft of the experiment on the upper surface. Like the 1 Hz case, the real component of pressure near the upper surface shock is lower in amplitude and aft of the experimental peak. On the lower surface, the mean of the computations shows good agreement with the experimental data everywhere, including the position and amplitude of the shock peak. For this higher frequency case, the experimental data shows a larger imaginary component of pressure response, particularly near the upper surface shock. Again, the mean of the computations show a shock location that is aft of the experimental peak, but the peak amplitude is close to the experimentally measured values. It is reiterated that it is impossible to predict the precise location and magnitude of the experimental peak due to the likelihood that a pressure sensor is not located on the peak. Away from the upper surface shock, overall character of the out-of-phase pressure component compares very well with the experimental data.

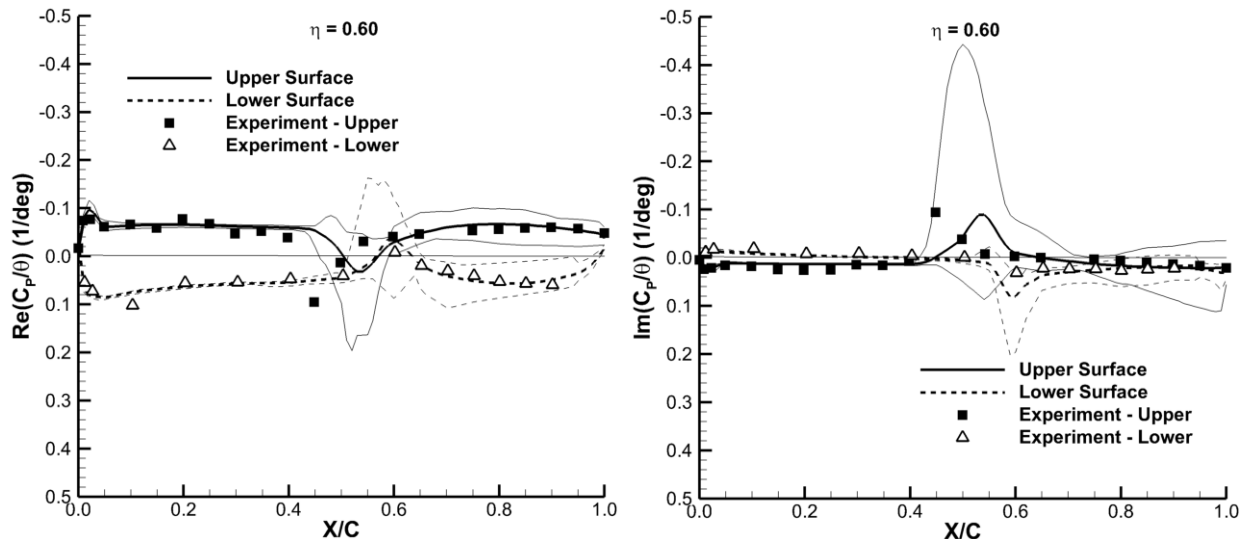


Figure 14. BSCW unsteady pressure comparison $M = 0.85$, $\alpha = 5^\circ$, $\theta = 1.0^\circ$, $f = 10$ Hz.

C. HIRENASD

The data selected for the HIRENASD wing investigated the steady and unsteady aerodynamic response to changes in Mach number and Reynolds number. Mean and fluctuating pressures were compared at $M = 0.70$ and $M = 0.80$ at $\alpha = 1.5^\circ$ and 7 million Reynolds number based on the wing reference chord. A higher Reynolds number case of 23.5 million at $M = 0.80$ and $\alpha = -1.34^\circ$ was also investigated. Unlike previous cases where the wing was oscillated in pitch, the unsteady motion for HIRENASD was generated by exciting the wing second bending mode near its natural structural frequency. The sections shown for comparison in the following figures were chosen to be near the anti-node of the second bending mode where the wing deformation would be largest. Since the model is effectively clamped at its wing root, the deflection at the inboard anti-node will be smaller than the deformation at the outboard station. The fluctuating pressure response is scaled by the maximum deflection of the wing measured at a point near the wing tip. This tip deflection, along with the frequency of oscillation, is listed in Table 3. AePW analysts chose to model the modal excitation in two ways: specified motion of the second bending mode with a prescribed frequency and amplitude, or through a fully aeroelastic simulation where the structural dynamics equations of motion are coupled with the aerodynamics and the model anchor point is oscillated similar to the approach used in the wind tunnel testing. Results from both approaches are included in the unsteady pressure comparisons presented below and no attempt is made to investigate result differences due to these varied approaches.

The steady cases will be reviewed first. Figure 15 shows the comparison between the AePW analyst data and experiment for the $M = 0.70$, $\alpha = 1.5^\circ$, $Re = 7$ million steady case. The comparison between the analysts and the experiment is excellent for this subcritical case with the largest difference seen near the leading edge of the wing at the $\eta = 0.953$ span station. The envelope surrounding the mean of the computations is nearly indistinguishable at both span stations, indicating a high degree of consistency among the analysts.

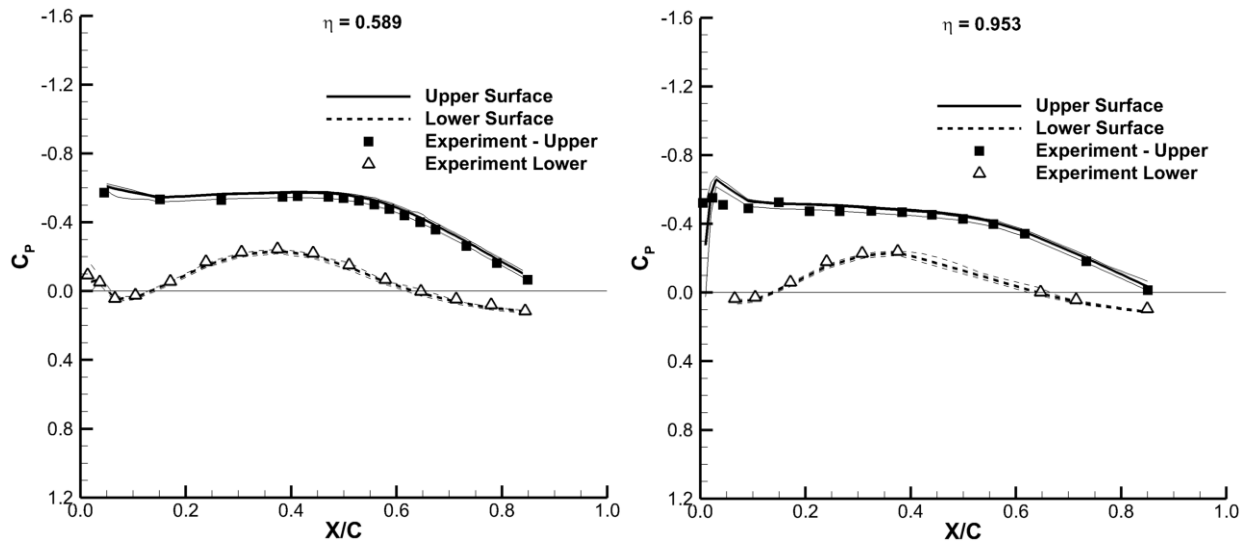


Figure 15. HIRENASD steady pressure comparison $M = 0.70$, $\alpha = 1.5^\circ$, $\Delta z = 0.0$ mm, $f = 0$ Hz, $Re = 7$ million.

Figure 16 present a similar comparison for the $M = 0.8$, $\alpha = 1.5^\circ$, $Re = 7$ million case. For this mildly transonic case, the comparison of the average of all the computations with the experimental data is generally very good. The majority of the calculations predict the upper surface flow recompression near 50% chord at the $\eta = 0.589$ station to be slightly aft of the experimental data. The computational envelope surrounding the average is larger for this case than for the previous case, particularly near and aft of the $\eta = 0.589$, 50% chord region on the upper surface. As seen with the previous RSW and BSCW cases, the analyses begin to show larger differences as shock and other transonic nonlinearities become more prevalent. The comparison on the lower surface of the wing is very good with the average of the computations strongly biased to one side envelope indicating that the vast majority of the computations agree very closely with only one or two outliers.

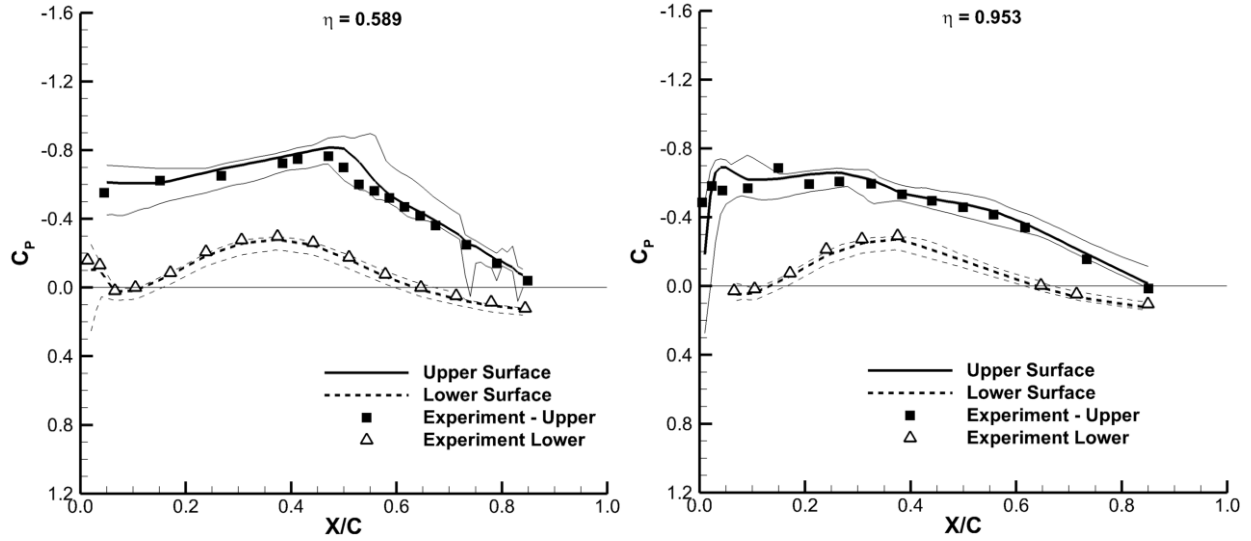


Figure 16. HIRENASD steady pressure comparison $M = 0.80$, $\alpha = 1.5^\circ$, $\Delta z = 0.0$ mm, $f = 0$ Hz, $Re = 7$ million.

The final steady case compares data in Figure 17 at $M = 0.80$, $\alpha = -1.34^\circ$, and $Re = 23.5$ million. The lower angle-of-attack for this case produces nearly zero net lift load on the wing and eliminates the mid-chord shock at the $\eta = 0.589$ station. The comparisons between the experimental data and the average of the computations are again very good everywhere and the calculations show very consistent results over the majority of the two stations examined. Near the leading edge of the inboard station, the envelope surrounding the computations expands in the area of the high flow acceleration on the wing lower surface.

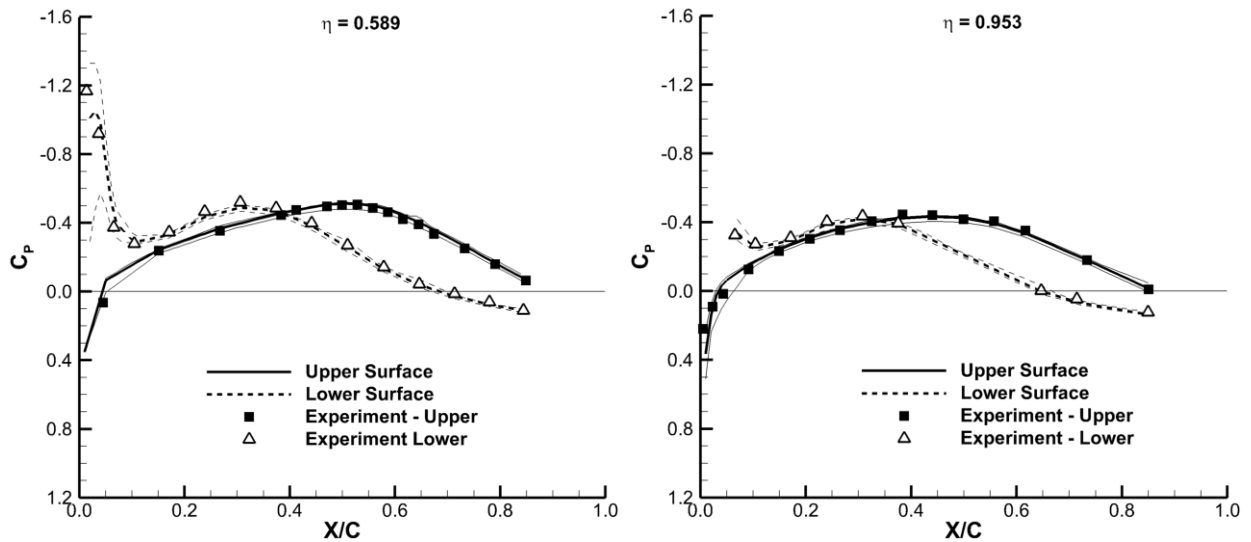


Figure 17. HIRENASD steady pressure comparison $M = 0.80$, $\alpha = -1.34^\circ$, $\Delta z = 0.0$ mm, $f = 0$ Hz, $Re = 23.5$ million.

Fluctuating pressure comparisons are shown in Figure 18 for the $M = 0.70$, $\alpha = 1.5^\circ$, $Re = 7$ million unsteady case. In this example, the oscillation amplitude is $\Delta z = 2.0$ mm and the frequency of oscillation is $f = 79.3$ Hz. Like the steady counterpart shown in Figure 15, the comparison between the theory and experiment is excellent for both the real and imaginary fluctuating pressure components at both wing stations. The consistency among the methods is also very good with only minor expansion in the computational envelope near the upper surface leading edge on the outboard station.

There are a number of interesting physical characteristics that can be derived from these plots that further reinforce the ability of the computational methods to accurately predict this type of aeroelastic problem. Since the second bending mode is being excited in this analysis and pressures are being compared at the anti-nodes of the mode, the 180° phase shift in the motion between the $\eta = 0.589$ and $\eta = 0.953$ stations can be readily observed in the pressure distributions. At these stations under the second bending mode, the airfoil sections are effectively undergoing a plunging motion and as a result generating an induced local angle-of-attack at the wing section. While the tip station is moving upward and inducing a negative angle-of-attack, the inboard station is moving downward and inducing a positive angle of attack, and vice versa. This is observed in the pressure distributions of Figure 18 by the swapping in orientation of the upper and lower surface pressures between the inboard and outboard stations. At the outboard station where the wing section moves up in phase with the prescribed motion, a negative induced angle-of-attack is generated and the lower surface pressures are primarily negative while the upper surface pressures are positive, indicating negative sectional lift. At the inboard station, the wing section moves down 180° out of phase with the upward tip motion and produces a positive induced angle-of-attack and sectional lift as evidenced by the upper surface pressures being primarily negative and lower surface pressures primarily positive.

Since the inboard station is nearer the clamped end of the mode shape, the amplitude of the vertical motion at this location is smaller than at the tip. Thus the induced angle-of-attack inboard will be smaller than at the outboard station. This is seen in the overall smaller magnitudes of the fluctuating pressure on the inboard station versus the outboard station. Finally there is a second, more subtle phase shift between the inboard and outboard station that is observed when examining the relative magnitudes of the real and imaginary fluctuating pressure components. At the inboard station, the imaginary component of the pressure distribution is generally larger than the real component, indicating that the inboard pressures respond nearly 90° out-of-phase with the wing motion. At the outboard station however, the opposite is observed with the real component of the pressures being generally larger than the imaginary component, which says the pressure respond nearly directly in-phase with the structural motion. This second bending mode oscillation produces a complex aerodynamic-structural interaction, the features of which are very accurately captured by the computational methods for this case.

Figure 19 shows a markedly different picture for the $M = 0.80$, $\alpha = 1.5^\circ$, $Re = 7$ million unsteady case. The amplitude of oscillation for this case is $\Delta z = 2.4$ mm and the frequency of oscillation is $f = 78.9$ Hz. As in the steady case, when transonic nonlinearities are added to the computations, the predictions begin to differ substantially among each other as well as from the experimental data. For this case, the lower surface pressures are closely predicted by most of the computations at both the wing stations. The fact that the average and one side of the lower surface envelope is very close to the experimental data justifies this claim with only one or two analyst submissions defining the far side of the envelope. The upper surface computations do not show this consistency however, with a large spread in the envelope on either side of the average and across virtually the entire upper surface. There is a shock on the upper surface near 50% chord on the inboard wing station that is captured in both the experimental data and by the computations. The computational position of the shock is aft of the experimental data as observed in the previous comparisons depicting transonic flow. At the outboard station, the upper surface average pressure comparison with the experimental data in the 10%–40% chord region is poor, but improves beyond 40% chord. However, the envelope on both sides surrounding the average is large across the entire chord length showing that there is a significant amount of variation among all the methods. At both stations, the general character of the upper surface pressures is captured for this case, but the differences between the computations and experiment are considered large, especially on the outboard station.

Figure 20 compares the fluctuating pressures at $M = 0.80$, $\alpha = -1.34^\circ$, and $Re = 23.5$ million. The amplitude of oscillation for this case is $\Delta z = 0.9$ mm and the frequency of oscillation is $f = 80.4$ Hz. The reduced mean angle-of-attack for this case eliminates the upper surface shock on the wing and minimizes transonic nonlinearities in the flow, except near the lower surface leading edge. The consistency of the computations for this case is much improved over the previous case with the largest envelope around the mean occurring near the wing leading. The comparison with the experimental data is also very good for this set of conditions. The computations are in good agreement with the experimental data everywhere except near the lower surface leading edge on the inboard wing

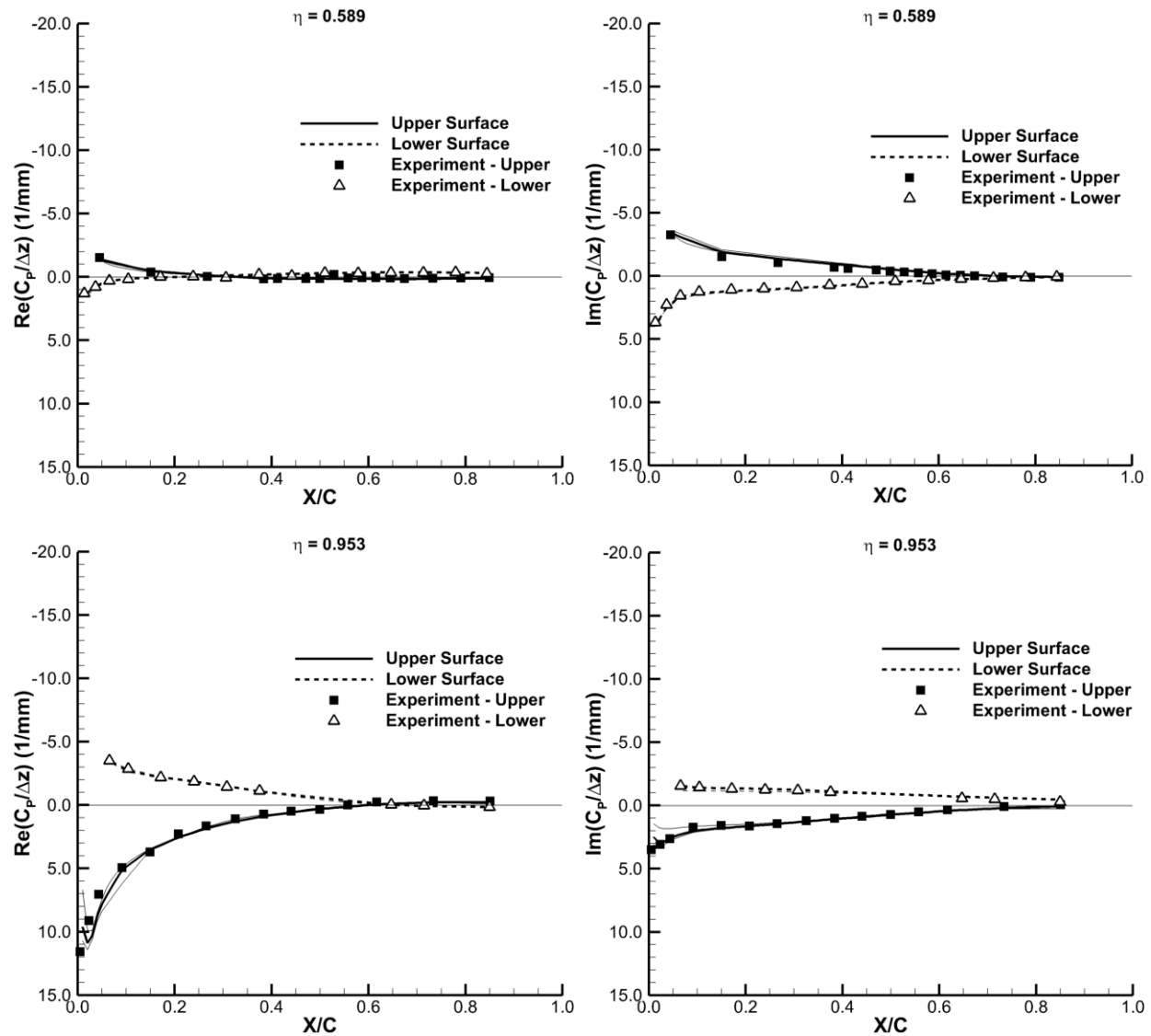


Figure 18. HIRENASD unsteady pressure comparison $M = 0.7$, $\alpha = 1.5^\circ$, $\Delta z = 2.0$ mm, $f = 79.3$ Hz, $Re = 7$ million.

station. Even in this region however, the overall character of the real and imaginary pressure components is well-predicted, but the peak in the pressure distribution is low for all the submitted computations. The reader is reminded that all but one of the analysts submitted their data only at the experimental pressure port locations. In high pressure gradient regions like this, the actual computed peak pressure could occur between the experimental data points and the actual peak pressure magnitude could be much larger than that portrayed in the plots. Also, a small forward or aft shift in the computed pressure peak could result in large differences at the experimental locations when the pressure gradients are very large. This is especially the case near the inboard lower surface leading edge.

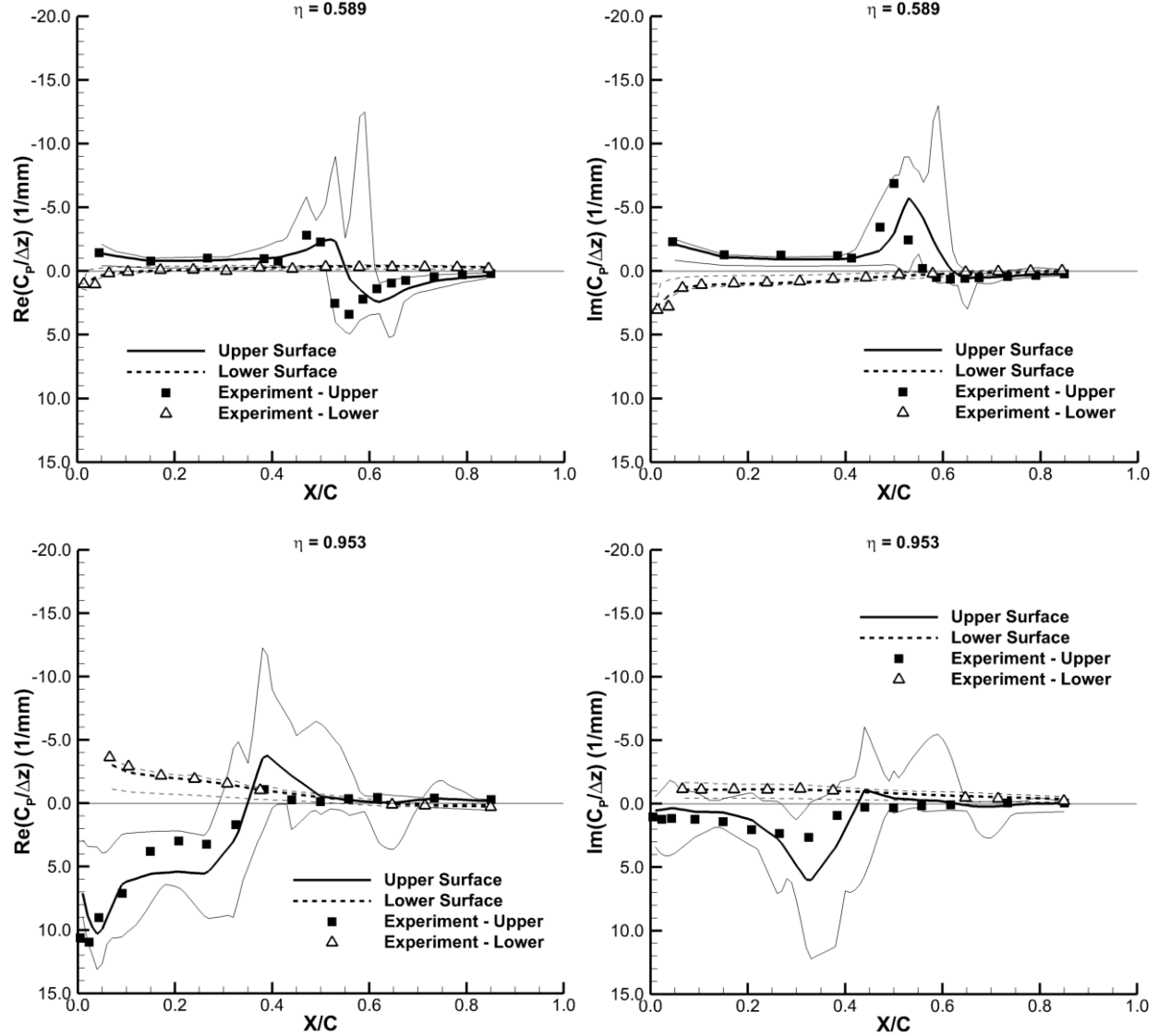


Figure 19. HIRENASD unsteady pressure comparison $M = 0.8$, $\alpha = 1.5^\circ$, $\Delta z = 2.4$ mm, $f = 78.9$ Hz, $Re = 7$ million.

III. Conclusion

A thorough comparison of the steady and unsteady pressure data from computations submitted to the first Aeroelastic Prediction Workshop has been performed and presented in this paper. Data from three different test cases, each with its own specific set of objectives to assess the state-of-the-art of computational aerodynamics in predicting nonlinear unsteady aerodynamics has been collected and analyzed. The rectangular Supercritical Wing was chosen for its geometric simplicity and relatively benign transonic flow conditions. Complications in the experimental setup for this wing that were not recognized prior to its selection as a test case severely complicated the analysis of this wing and very likely contributed to the poor performance of the computational methods for this problem, especially at the inboard wing station. The Benchmark Supercritical Wing test case presented a simple geometry with a set of flow conditions that were expected to be very challenging to the computational tools and it did not disappoint. Proper grid refinement proved to be essential in performing the calculations at the static angle-of-attack required as initial conditions for the unsteady time domain analyses. Grids that were too coarse did not exhibit the unsteady flow character that was present for this case, even though the wing was fixed at a steady angle-

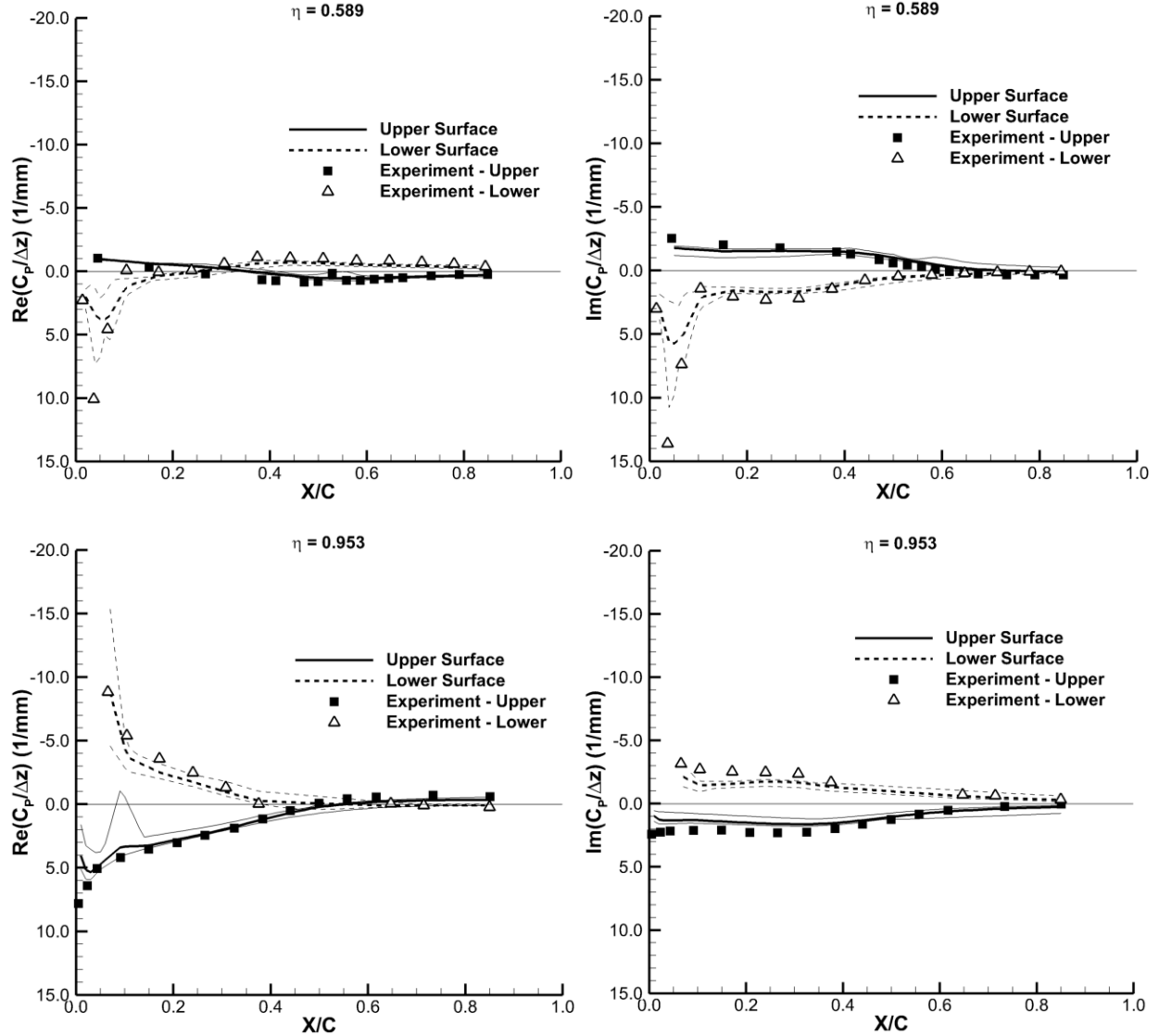


Figure 20. HIRENASD unsteady pressure comparison $M = 0.8$, $\alpha = -1.34^\circ$, $\Delta z = 0.9$ mm, $f = 80.4$ Hz, $Re = 23.5$ million.

of-attack. Regardless of the fact that some analysts did not predict the initial unsteadiness at the fixed angle-of-attack, the unsteady computations exhibited remarkable consistency everywhere except near and behind the shock. Variations in the computations were large in these regions and the predicted shock location was generally aft of the experiment. The HIRENASD wing provided the most geometrically and mechanically complex test case, but it also provided the most consistent set of computational results and comparisons with experimental data as long as the flow conditions were not highly transonic. The subcritical $M = 0.70$, $\alpha = 1.5^\circ$, $Re = 7.0$ million and $M = 0.80$, $\alpha = -1.34^\circ$, $Re = 23.5$ million cases showed good comparison with the experimental data and good consistency among the computations. The transonic $M = 0.80$, $\alpha = 1.5^\circ$, $Re = 7.0$ million case proved to be considerably more difficult for the analysts. This appears to be the general theme of the overall analysis for all the test cases. The computational methods seem to perform very well for problems and areas of the flow that are linear, but nonlinearity in the form of shock waves, shock-boundary layer interaction, flow separation, and other viscous interactions challenge both the steady and unsteady calculations. It is not clear how the accuracy of the steady calculation used as an initial condition for the unsteady analysis affects the accuracy of the unsteady computations, but logic says it must be a significant contributor. There is also the open question of how small errors in the initial conditions can affect the

unsteady computations for highly nonlinear transonic flows. A partial answer to this question may be embedded in the data acquired in this first installment of the AePW, but that analysis is beyond the scope of this paper.

The AePW analysts are continuing to compute and analyze at least the BSCW and HIRENASD configurations. The complexity of the RSW experimental setup up coupled with the age and availability of the experimental data for this case likely limits the value of future analysis for this configuration. The shock-buffet character of the BSCW at steady angle-of-attack has attracted the attention of several workshop participants that did not initially analyze this configuration and are now interested in testing their methods on it. HIRENASD has the most attractive and relevant geometry of the test cases evaluated and it has a very large and detailed experimental database available. There are a vast amount of test conditions and flow phenomena investigated in this experiment and it should continue to be an excellent resource for unsteady aerodynamic and aeroelastic analysis for quite some time.

IV. References

- ¹Heeg, J., et al., "AEPW Overview Paper"
- ²Levy, David W., et al., "Summary of Data from the First AIAA CFD Drag Prediction Workshop," AIAA Paper AIAA-2002-0841, January 2002.
- ³Rumsey, et al., "Summary of the First AIAA CFD High Lift Prediction Workshop," AIAA Paper AIAA-2011-0939, January, 2011.
- ⁴Heeg, J., et al., "Plans for an Aeroelastic Prediction Workshop," IFASD-2011-110, International Forum on Aeroelasticity and Structural Dynamics, June 2011.
- ⁵Ricketts, R., et al. "Geometric and Structural Properties of a Rectangular Supercritical Wing Oscillated in Pitch for Measurement of Unsteady Pressure Distributions," NASA TM-85763, November 1983.
- ⁶Ricketts, R., et al., "Transonic Pressure Distributions on a Rectangular Supercritical Wing Oscillating in Pitch," NASA TM-84616, March 1983.
- ⁷Ricketts, R., et al., "Subsonic and Transonic Unsteady and Steady-Pressure Measurements on a Rectangular Supercritical Wing Oscillated in Pitch," NASA TM-85765, August 1984.
- ⁸Bennett, R. M. and Walker, C. E., "Computation test Cases for a Rectangular Supercritical Wing Undergoing Pitching Oscillations," NAS TM-1999-209130, April 1999.
- ⁹Dansberry, B.E.; et al., "Physical Properties of the Benchmark Models Program Supercritical Wing," NASA TM-4457, September 1993.
- ¹⁰Dansberry, B. E., "Dynamic Characteristics of a Benchmark Models Program Supercritical Wing," AIAA Paper AIAA 92-2368, April 1992.
- ¹¹Piatak, D. J. and Cleckner, C. S., "Oscillating Turntable for the Measurement of Unsteady Aerodynamic Phenomenon," *Journal of Aircraft*, Vol. 14, No. 1, Jan. – Feb. 2003.
- ¹²Ballman, et al., "Experimental Analysis of High Reynolds Number Aero-Structural Dynamics in ETW," AIAA Paper AIAA-2008-0841, January 2008.
- ¹³Dafnis, A., et al. "Dynamic Response of the HiReNASD Elastic Wing Model under Wind-Off and Wind-On Conditions", International Forum on Aeroelasticity and Structural Dynamics, IF-073, 2007.
- ¹⁴Ballmann, J., et al. "Aero-structural wind tunnel experiments with elastic wing models at high Reynolds numbers (HIRENASD-ASDMAD)", AIAA Paper AIAA-2011-0882, January 2011.
- ¹⁵Reimer, L., et al., "Computational Aeroelastic Design and Analysis of the HiReNASD Wind Tunnel Wing Model and Tests", International Forum on Aeroelasticity and Structural Dynamics, IF-077, 2007
- ¹⁶Reimer, L., Ballmann, J., and Behr, M., "Computational Analysis of High Reynolds Number Aerostructural Dynamics (HiReNASD) Experiments," IFASD-2009-132, International Forum on Aeroelasticity and Structural Dynamics, 2009.
- ¹⁷Neumann, J., and Ritter, M., "Steady and Unsteady Aeroelastic Simulations of the HIRENASD Wind Tunnel Experiment," IFASD-2009-132, International Forum on Aeroelasticity and Structural Dynamics, 2009.
- ¹⁸Neumann, J., Nitzsche, J., and Voss, R., "Aeroelastic Analysis by Coupled Non-linear Time Domain Simulation," RTO-MP-AVT-154, 2008.
- ¹⁹AePW Lessons Learned Paper for RSW.